

Use of Reciprocal Lattice Layer Spacing in Electron Backscatter Diffraction Pattern Analysis

J. R. Michael¹ and J. A. Eades²

¹ Sandia National Laboratories, P. O. Box 5800, Albuquerque, NM 87185-1405

² Dept. of Materials Science and Engineering, Lehigh University, Bethlehem, PA 18015-3195

ABSTRACT

In the scanning electron microscope (SEM), using electron backscattered diffraction (EBSD), it is possible to measure the spacing of the layers in the reciprocal lattice. These values are of great use in confirming the identification of phases. The technique derives the layer spacing from the HOLZ rings which appear in patterns from many materials. The method adapts results from convergent-beam electron diffraction (CBED) in the transmission electron microscope (TEM). For many materials the measured layer spacing compares well with the calculated layer spacing. A noted exception is for higher atomic number materials. In these cases an extrapolation procedure is described that requires layer spacing measurements at a range of accelerating voltages. This procedure is shown to improve the accuracy of the technique significantly. The application of layer spacing measurements in EBSD is shown to be of use for the analysis of two polytypes of SiC.

PACS: 07.78, 61.16.B, 61.14, 61.14L

Keywords: Electron Diffraction, Scanning Electron Microscopy, Electron Backscattering Diffraction

INTRODUCTION

Electron backscattering diffraction (EBSD) in the scanning electron microscope (SEM) is rapidly becoming a standard technique for the crystallographic analysis of micrometer sized regions of bulk specimens. EBSD had primarily been used as a tool for the mapping of the crystallographic orientation of a known polycrystalline sample [1,2]. A newer use of EBSD is for the identification of unknown crystalline phases in bulk specimens [3,4]. It is for this application that the use of higher order Laue zone (HOLZ) rings to determine the reciprocal lattice layer spacing may be most helpful [5].

EBSD patterns are formed by the elastic scattering or channeling of inelastically scattered electrons. The patterns appear as though the electrons that contribute to the pattern diverge from a point source of radiation within the sample and are therefore termed divergent beam diffraction patterns [6]. EBSD patterns are related by reciprocity to channeling patterns or rocking beam patterns from bulk specimens. Many of the features observed in EBSD patterns are also observed in CBED patterns. However, there is only an approximate relationship between EBSD patterns and CBED patterns because the geometry is different in the two cases [7]. EBSD patterns in the SEM consist of pairs of Kikuchi lines that intersect at zone axes. In addition to the prominent Kikuchi bands and

DISCLAIMER

Portions of this document may be illegible in electronic image products. Images are produced from the best available original document.

lines, there may also be rings observed round the zone axes. These HOLZ rings correspond to an envelope of excess lines paired with deficiency lines excited close to the zone axis, but where the reciprocal lattice point is not in the zero layer.

Attempts to perform phase identification strictly through the determination of lattice spacings from the Kikuchi bands have been unsuccessful due to the inherent inaccuracies in the measurements. Also, it is very difficult, if not impossible, to obtain accurate measurements of planes whose spacing is greater than about 0.5 nm due to the dynamic nature of the patterns and the overlap of the line pairs leading to difficulties in measuring their spacing. Phase identification using EBSD is possible if the angles between the Kikuchi bands and the d-spacing for each Kikuchi band are combined to calculate a unit cell volume. This unit cell volume when combined with the qualitative chemistry of the sample can be used to search a crystallographic database for appropriate matches and identification [8]. This technique is limited to the compounds that appear in the database. The use of HOLZ rings to determine reciprocal lattice layer spacings may be used as a verification of the identification and may be useful for the determination of the crystallography of phases that do not appear in the database provided sufficient accuracy can be obtained.

It is well known that the diameter of the HOLZ rings in convergent-beam electron diffraction (CBED) in the transmission electron microscope is determined by the spacing of the reciprocal lattice planes perpendicular to the direction of the particular zone axes studied. There have been many studies of this type and the error in reciprocal lattice spacing has been shown to be generally no better than 1-2 % as a result of lens distortions that accompany the short camera lengths used to image HOLZ rings in CBED [9,10]. We are aware of no studies that have attempted to make use of the HOLZ rings that are visible in EBSD patterns. There has been some speculation that the measurement of reciprocal lattice layer spacings should be possible, but the nature of the gnomonic projection may make this extremely difficult and tedious [5].

The technique usually employed in TEM is to measure the diameter of the HOLZ ring as a length in reciprocal space and then use the approximation:

$$G^2 = 2kH \quad 1$$

where G is the diameter of the HOLZ ring, k is the reciprocal of the electron wavelength and H is the spacing of the reciprocal lattice in the direction of the zone axis [10]. In the case of EBSD it seems natural to measure the diameter of the ring in terms of angle. One of the main reasons for this is that EBSD patterns are gnomonic projections and therefore distances or angles measured on the pattern are not correct unless the gnomonic projection is accounted for. If we define the radius of the HOLZ ring as 2θ then from geometry we obtain:

$$H = k(1 - \cos 2\theta) = 2k(\sin^2 \theta) \quad 2$$

If we employ the small angle approximation, both equations 1 and 2 reduce to :

$$H = 2k\theta^2 = \frac{k(2\theta)^2}{2} \quad 3$$

In this study, equation 2, the exact geometrical calculation will be used to calculate the layer spacings. The errors introduced by the small angle approximation are small and for angle up to 10° are less than 1 part in 1000.

The measurement of the layer spacing in the reciprocal lattice through the use of the above equations requires no prior knowledge of the crystal structure, unit cell dimensions or orientation. If the crystal structure and the specific zone axis [uvw] are known, it is possible to use simple analytical equations to calculate the reciprocal layer lattice spacing [10]. The layer spacing may be calculated using:

$$H^{-1} = \left[(au)^2 + (bv)^2 + (cw)^2 + 2abuv \cos\gamma + 2bcvw \cos\alpha + 2cwu \cos\beta \right]^{1/2} \quad 4$$

where a, b, c are the lattice parameters and α , β , γ are the angles between the unit cell axes. This equation is correct for primitive unit cells, but it does not take into account extinctions that are caused by cell centering. Equation 4 will always provide the largest layer spacing and if there are extinctions present the measured value will always be related to the calculated value by an integer multiple. As an example, for the primitive hexagonal cell there are allowed reflections in each higher order Laue zone so there are no missing planes in the reciprocal lattice. However, in a rhombohedral cell the first and second zones contain only forbidden reflections and therefore will not be observed. Only the zero and the third zones will be present. Since two out of the three zones are missing equation 4 will calculate a layer spacing that is three times larger than the measured spacing. This is true for higher order zone axes, but higher symmetry axes such as [001] and [110] have allowed reflections in all the zones and therefore all of the zones will be observed [9,10, 11].

This paper will first demonstrate that HOLZ rings can be easily observed in EBSD patterns and that these rings can, in some cases, be used to measure the spacing of planes in the reciprocal lattice. The limits of this analysis will then be discussed and some techniques to improve the accuracy of the measurement will be discussed.

EXPERIMENTAL

The patterns analyzed in this study were collected using a CCD-based camera system that was mounted on a JEOL 6400 SEM. The SEM was equipped with a LaB_6 electron source that could be operated at a range of accelerating voltages up to 40 kV. The camera system consisted of a single crystal Ce doped yttrium aluminum garnet (YAG) phosphor, fiber optically coupled to a 1024 X 1024 pixel scientific-grade slow-scan charge coupled device (CCD) array. The CCD was thermoelectrically cooled to -20°C . The SEM was operated at a range of beam currents that permitted patterns to be collected

in 5 to 10 seconds of exposure. The camera was calibrated using procedures described previously [4].

The patterns were flat fielded to reduce the background and to increase the contrast. Flat fielding was accomplished by first collecting the pattern from the area of interest. This image contained crystallographic information, the slowly varying background due to the nature of the backscattered electron distribution from the tilted sample and artifacts from the camera. A second image was acquired using the same acquisition parameters while the electron beam was scanned over a number of grains. This procedure produced an image that contained the background variation and the camera artifacts, but without any of the crystallographic information. This is called the flat field image. The pattern containing the crystallographic information was normalized by the flat field image to produce the final image.

The pure metal and alloy samples used in this study were prepared using standard metallographic procedures. The samples were chemically etched after polishing to remove any small amounts of surface damage that may have been left after the mechanical polishing. The mineral samples were simply cleaned and then mounted in the microscope so that the crystal facet of interest faced the phosphor screen and at a relatively steep angle with respect to the electron beam. The actual surface tilt angle is not important in these studies as we are not calculating the exact specimen orientation.

The HOLZ rings were measured in at least four positions around the ring using the software program NIH Image. The actual angular diameter or radius of the ring must then be calculated using the calibrations for the camera. This is accomplished in the following manner. The angle between any two vectors ($x_1 y_1 z_1$ and $x_2 y_2 z_2$) in the pattern may be simply calculated as:

$$\cos\theta = \frac{(x_1 \cdot x_2 + y_1 \cdot y_2 + z_1 \cdot z_2)}{|x_1 y_1 z_1| |x_2 y_2 z_2|} \quad 5$$

where the x and y components of the vectors are relative to the pattern center and $z_1 = z_2$ is the camera length obtained from the calibration [1].

RESULTS

Figure 1 shows a typical pattern obtained from the mineral arsenopyrite (AsFeS , monoclinic) collected at 20 kV from a face of a euhedral crystal. There are a large number of HOLZ rings visible in the pattern. These HOLZ rings are not as high in contrast as those normally observed in CBED patterns in the TEM at higher accelerating voltages. The rings are not entirely made up of excess lines as half of each ring is bright and the other half is dark relative to the average intensity in the pattern. This supports the idea that these rings are produced by an envelope of excess and defect lines that sum together to produce the visible ring. It should be noted that HOLZ rings were not visible in EBSD patterns for every sample imaged. Figure 2 shows a pattern obtained from the mineral galena (PbS , cubic). There are few if any HOLZ rings visible in this pattern.

Table 1 shows a comparison of measured (at 20 kV) and calculated layer spacings for all seven basic crystal systems. For many of the examples shown in Table 1 there is very good agreement between the layer spacings measured from the EBSD patterns and the values calculated from the known crystal structures using equation 4 and taking into account any systematic extinctions. There are a number of interesting observations that can be made from the data shown in Table 1. First, it is apparent that the technique underestimates the actual layer spacing in all but four cases. Second, as the atomic number of the sample increases, the accuracy of the technique decreases. This can be most easily seen when one compares the data for W, Ta and Mo. The third interesting observation is that data taken from different zone axes result in apparently different accuracy. This is noted for the W and Mo data where the lower symmetry zone axis shows better accuracy than the higher symmetry zone axis data.

To assess some of the sources of experimental error an EBSD pattern was obtained from Cr_7C_3 in a high Cr steel and this pattern is shown in Figure 3. The phase was first identified as Cr_7C_3 (hexagonal, $a=0.7015$ nm, $c=0.4532$ nm). The zone axis in the upper left portion of the image is $[001]$ and there is a clear HOLZ ring visible about this zone axis. The results of the measurement of this HOLZ ring are shown in Table 2. The average of these measurements is 0.453 ± 0.003 nm (standard deviation of the measurements) which is in excellent agreement with the calculated value of 0.453 nm.

The experimental errors in the above measurements are difficult to assess due to the nature of the gnomonic projection. The angle subtended by a given pixel in the CCD array varies with the distance of the pixel from the pattern center. A single pixel at the pattern center subtends an angle of 0.17° while a pixel at the edge of the pattern subtends an angle of 0.086° . Thus, the error in the measurement of the HOLZ ring radius is related to the position of the ring with respect to the pattern center. Since the calculation of the ring diameter requires the pattern center to be known, errors in the pattern center position will cause errors in the diameter calculation. In the example shown in Table 2, the error caused by a shift in the pattern center of one pixel in x resulted in a change in the layer spacing measurement of 0.001 nm. An uncertainty in the camera length of a distance equivalent to one pixel resulted in a change in the measured layer spacing of 0.002 nm. These errors resulting from errors in the calibration of the pattern center and camera length are relatively small. The other source of error is the actual measurement of the ring position. Again in the example shown in Table 1, a change of one pixel in the position of the HOLZ ring results in an error of 0.089° in the angle and 0.0074 nm in the layer spacing. Other HOLZ rings that are closer to the pattern center will show slightly larger changes in measured layer spacing and those further away from the center will show smaller errors. The careful calibration of the system used in these experiments has shown that angles can consistently be measured to better than 0.1° . Therefore, it is not likely that the calibration is contributing much to the measurement uncertainty. The absolute measurement of the position of the HOLZ ring is most likely the largest source of error. As can be seen from the Cr_7C_3 pattern in Figure 3 or the hematite patterns in Figure 4, the HOLZ rings may not be extremely sharp. This lack of sharpness leads to an

error in the measurement of the absolute position of the ring and thus introduces an error that may be as large as 0.007 nm.

To assess the HOLZ layer spacing measurement over a range of voltages a sample of Hematite (Fe_2O_3 , trigonal) was imaged at beam energies from 5 to 30 kV. These patterns are shown in Figure 4a-e. Note that the positions of the zone axes do not change with kV only the Bragg angle for each plane and the diameter of the HOLZ rings changes. The HOLZ ring diameter decreases with increasing accelerating voltage as expected. Table 3 shows the measured reciprocal lattice layer spacings for the [211] zone axis. The layer spacing, calculated using equation 4 and the unit cell parameter for hematite, for this zone axis is 0.5427 nm. The experimental data agrees quite well with this value for a wide range of accelerating voltages (5 to 30 kV).

In order to determine both the effect of atomic number and microscope accelerating voltage, samples of Mo and W were prepared. These metals are body centered cubic and have lattice parameters of 0.3165 nm for W and 0.3147 nm for Mo. Figure 5 a-c and Figures 6 a-c are the patterns obtained from Mo and W at 10, 20 and 35 kV for Mo and 10, 20 and 40 kV for W. The measured layer spacings as a function of microscope accelerating voltage are shown in Table 4 for Mo and Table 5 for W. Compared with the results shown for Cr_7C_3 and hematite, the measurements do not agree well with the expected values. However, it is clear that as the accelerating voltage is increased the measured layer spacing decreases toward the calculated value. Table 6 shows the measured layer spacings as a function of accelerating voltage for the W [100] zone axis. It is interesting to note that the measured layer spacing decreases toward the correct value for the Mo and W [111] with increasing accelerating voltage. The data for the [100] generally shows the same trend with the exception of the 40kV data.

DISCUSSION

The results for Cr_7C_3 and hematite and many of the examples shown in Table 1 demonstrate that HOLZ rings can be used to determine the reciprocal lattice layer spacing. The accuracy of the measurements in these two cases are very good and are equal to or better than those that can be achieved in CBED in the TEM. This increased accuracy is mainly due to the complete lack of lens distortions in the EBSD case in the SEM when compared to CBED in the TEM [9]. Thus, layer spacing measurement using HOLZ rings in EBSD patterns is viable and can be used for the identification of crystalline phases. However, there are examples shown where the measurement of the HOLZ ring diameter results in very poor accuracy.

The measured layer spacings for W and Mo are not nearly as accurate as those shown for Cr_7C_3 , hematite and some of the other examples in Table 1. Examination of the data shown in Table 4, 5 and 6 shows that higher accelerating voltages produce more accurate results. Also, it is apparent from data shown in Table 1, that lower symmetry zone axes also result in better accuracy. These results may indicate that the dynamical nature of the diffraction in these patterns requires more than the simple calculation shown in equation

2. Unfortunately, it is difficult to know a priori how close the measured value from the EBSD patterns will come to the actual layer spacing separation. Thus, when a new sample is under study, it is important that the analysis be performed at two different accelerating voltages as a check. If the measurements are within experimental error, then it is safe to assume that the simple calculation shown in equation 2 is adequate. However, if the data show a variation with accelerating voltage the following procedure must be applied to improve the results.

When equation 2 is used to calculate the separation of the layers in reciprocal space the value calculated is the kinematic value, but the experimental value will be different due to dynamical effects. If we call H_a the apparent value that we measure, then the true value H is related to the apparent value by:

$$H_a = H - \Delta H \quad 5$$

where

$$\Delta H = \frac{f}{\xi} \quad 6$$

and f is a geometrical factor and ξ is the extinction distance. Please see the Appendix for the derivation of equation 6 and 7. Two-beam extinction distances scale with the electron velocity. If we assume that the many-beam extinction distance at the zone axis scales the same way and use a non-relativistic expression for the energy we can now write an expression that shows:

$$\Delta H = \frac{C}{E^{1/2}} \quad 7$$

where C is some constant and E is the energy of the electron. Equation 7 along with equation 5 imply that a plot of measured H spacing vs. $1/E^{1/2}$ will have a y-intercept that is closer to the actual H spacing.

A plot of the measured layer spacing vs. $1/(E)^{1/2}$ is shown for Mo at [111] in Figure 7. A linear fit to the data results in a y-intercept of 3.683 nm^{-1} with a correlation coefficient of 0.95. The calculated value for Mo is 3.668 nm^{-1} or about a 0.4% difference. A plot of the data for W at [111] shown in Table 4 yields a y-intercept of 3.408 nm^{-1} and a correlation coefficient of 0.99. The calculated value for W is 3.648 nm^{-1} or a difference of 6.6%. This result for W is in closer agreement to the actual value than the measurements, but is not as close as the Mo data. The interpretation of the W [001] data is not as clear. The value at 40 kV is within the experimental error of the value measured at 20 kV. If the 10 and 20 kV data are extrapolated the result is a layer spacing of 2.90 nm^{-1} which is about 8% smaller than the calculated value of 3.16 nm^{-1} . There are a number of possibilities for the similarities of the 20 and 40 kV data and the poor results of the extrapolation. First, it is possible that there is a shift to a different branch of the dispersion surface at 40kV. This will lead to errors in the extrapolation as it does not take into account these shifts. It is also possible that the extrapolation procedure is too simplistic for the very short

extinction distances expected at strong zone axes in W . It is also possible that the assumption of a constant C in equation 7 is not exact.

It has been suggested for CBED that layer spacing measurements from HOLZ rings could be very useful for polytype identification [9]. This is based on the limited angular view ($<15^\circ$) that is normally achieved in CBED allowing only one zone to be imaged in a single pattern. A properly designed EBSD camera can achieve an angular view of over 90° , thus obviating the need to use HOLZ ring measurements to perform polytype identification. However, it is still useful to use the HOLZ ring measurements to verify the proper identification of a phase and the proper indexing of the pattern. Figure 8 shows patterns collected from two polytypes of SiC. The pattern shown in Figure 8a is from the 6H polytype (hexagonal $a=0.3073$ $c=1.508$ nm) and Figure 8b is from the SiC 15R polytype (rhombohedral $a=0.3073$ $c=37.70$ nm). Upon inspection of the patterns it is fairly easy to recognize that the symmetry about the zone axis marked [001] is six-fold in the case of Figure 8a and three-fold in the case of Figure 8b in agreement with the known crystal structures of the polytypes. The automatic indexing software had little difficulty in identifying the correct polytypes for figure 8a and b. The indexed patterns are shown in Figure 8c and d. The HOLZ rings labeled [241] in Figure 8a and [10 5 1] in Figure 8b were used to verify the correct indexing of the patterns and the results are shown in Table 1. The HOLZ ring about the zone axis labeled [2 4 1] in Figure 8a was used and the measured layer spacing was 1.858 nm which is in excellent agreement with the calculated value from equation 3 of 1.846 nm. The HOLZ ring about the zone axis labeled [10 5 1] in Figure 8b was used and the measured layer spacing was 1.545 nm in good agreement with the calculated value of 1.538 nm. Thus the layer spacings verify that the polytypes have been identified correctly.

CONCLUSIONS

Reciprocal lattice layer spacings measured from HOLZ rings in EBSD patterns are comparable to calculated layer spacings within the experimental error for compounds with extinction distances that are not too short. It is difficult to know the extinction distance a priori and therefore the use of HOLZ rings in EBSD patterns requires that the measurement be performed using at least two different accelerating voltages. If these measurements are in agreement with each other then the effect of extinction distance may be ignored in most cases. If the results are not in agreement then the extrapolation technique developed in this study must be utilized to get a more accurate result. Also, the use of HOLZ rings round lower symmetry zone axes should produce better results. However, for high atomic number samples, the extrapolation technique does not appear to produce accuracy of much better than 10% and results obtained in this way should be used cautiously.

Acknowledgments

JRM would like to thank Ray Goehner and Eric Schlienger for helpful discussions. This work was supported by the United States Department of Energy under contract DE-ACO4-94AL8500. Sandia is a multiprogram laboratory operated by Sandia Corporation, a Lockheed Martin Company, for the United States Department of Energy.

Appendix

The displacement of the HOLZ ring from the kinematical position due to dynamical diffraction.

The kinematical radius of the HOLZ ring can be deduced from an Ewald sphere construction, as shown, for example, in figure A1. The electron beam is assumed to be incident on the sample at a zone axis orientation (normal to a plane in the reciprocal lattice). The diagram is drawn with the incident beam vertical as would be more appropriate for the transmission case than for the typical geometry of EBSD. However, this orientation has been chosen because it more readily relates to the conventions of the diagrams drawn for dynamical diffraction. Equations 1 and 2 of the main text can readily be deduced from this figure.

The position of the HOLZ ring is different if dynamical diffraction effects are strong. In that case, the Ewald sphere construction no longer predicts the correct position. The description given here is based on the work of Jones, et al. [12]. They showed that the position of HOLZ lines may be accurately described by treating the zero layer dynamically but treating the HOLZ interaction kinematically. The zero layer diffraction is represented graphically as a set of dispersion surfaces. In many cases only the first two branches of the dispersion surface are needed. In order to simplify the discussion, throughout this appendix, the wave vectors are taken to have been modified to take account of the mean inner potential.

Figure A2 shows the two branches of the dispersion surface, labeled (1) and (2). Then, inside the crystal, the wave vector of the electrons will be $k^{(1)}$ or $k^{(2)}$, rather than the k of the kinematical approximation. To discuss the HOLZ diffraction, we construct a sphere (S) centered on the HOLZ reflection. Then the HOLZ ring will appear at a position determined by the intersection of this sphere with the branches of the dispersion surface – intersections at positions A and B, in the figure. Kinematically, the HOLZ ring would appear in a position determined by the intersection marked X. The HOLZ ring will thus appear at an angle represented by one of the dashed lines instead of the continuous line between them. We suppose that the visible HOLZ ring is the one associated with the first branch of the dispersion surface. Then the HOLZ ring will be smaller than kinematical theory (as represented by equations 1 and 2 of the main text) would predict. Equation 2 of the main text is derived by writing, for an obvious triangle in figure A1,

$$\cos 2\theta = (k - H)/k. \quad A1$$

We can derive equation 1 in the text, which gives the same result expressed as a radius rather than an angle by applying Pythagoras theorem to the same triangle and neglecting second order terms.

$$G^2 = 2kH \quad A2$$

By considering a triangle in figure A2, we can see that dynamically the radius of the HOLZ ring is given instead by

$$\cos 2\theta = (k - H + \epsilon^{(1)})/k. \quad A3$$

The corresponding result in terms of radius, rather than angle, is:

$$G^2 = 2k(H - \epsilon^{(1)}) \quad A4$$

Thus, if we use the kinematic equations to calculate H we will get a value which is $H - \epsilon^{(1)}$, instead of the true value, where $\epsilon^{(1)}$ is the vertical separation between X and the first branch of the dispersion surface. (We have called this quantity $\epsilon^{(1)}$ following the terminology of Lin, et al. [13]. Bithell and Stobbs call this quantity $\gamma^{(1)}$ [14].) The separation between the two branches of the dispersion surface is $1/\xi$, where ξ is the many-beam extinction distance at the zone axis. $\epsilon^{(1)}$ is some fraction of this distance. The fraction in question will depend on the particular zone axis.

The result given (equation A3 and A4) is relatively trivial. Nonetheless, as far as we can establish it has not been given explicitly before. This may be because previous authors who have dealt with related topics have considered the transmission case where different factors are important.

Other researchers have done an analysis closely related to the one presented here [13,14]. However, they were concerned with the effect of dynamical diffraction on the positions of the HOLZ lines in the direct-beam, convergent-beam disc - not, as we are here, with the diameter of the HOLZ ring itself. They followed, as we do, the original paper by Jones, et al. [12].

The nearest we have found to this result is given by Bird [15]. He gives a relation for the spacing between two HOLZ rings (for the case when two branches of the dispersion surface produce visible effects). He does not give a result for the ring itself. His result in terms of the radius of the ring, rather than the angle :

$$\Delta G = \frac{1}{\xi} \sqrt{\frac{k}{2H}} = (\epsilon^{(1)} - \epsilon^{(2)}) \sqrt{\frac{k}{2H}}. \quad A5$$

In the paper the equation looks slightly different since he uses the convention that $k=2\pi/\lambda$, instead of $k=1/\lambda$. This result is consistent with (and may be derived from) the results given here (A4).

In summary the value of H determined from the kinematical equations will give a value which is too small by $\Delta H = \epsilon^{(1)}$. An exact value for $\epsilon^{(1)}$ would need to be calculated from a full dynamical simulation.

Lin et al. discuss the shift of HOLZ lines in the bright-field discs of convergent-beam patterns [13]. They use a description similar to that given here. They give an approximation for $\epsilon^{(1)}$ designed to avoid the need for a full many-beam dynamical calculation. They show that the shift of the lines associated with the first branch of the dispersion surface can be derived from $\epsilon^{(1)}$, using the approximation:

$$\epsilon^{(1)} = -\frac{1}{2k} \sum_{G \neq 0} \frac{|U_G|^2}{|G|^2} = \frac{2m^2 e^2}{kh^4} \sum_{G \neq 0} \frac{|V_G|^2}{|G|^2} \quad A6$$

with

$$U_G = V_G \frac{2me}{h^2} \quad A7$$

Here, k is the kinematical wavevector, V_G is the Fourier component of the crystal potential and the other symbols have their conventional meanings. The reciprocal lattice vectors are written G not g , to make clear that only the zero-order Laue zone is included. The energy dependence of $\epsilon^{(1)}$ is thus the energy dependence of $m^2/k = m^2\lambda$, since all the other terms are energy independent. Since relativistic effects are not very important at SEM beam energies, we will assume that m is energy independent – and that we can use the non-relativistic approximation for λ . Then the energy dependence of the error in H will be $E^{-1/2}$.

The apparent value of H_a (calculated from the kinematic equations) will be related to the correct value, H, by:

$$H_a = H - C/E^{1/2} \quad A8$$

where C is a constant.

References

- [1] S. I. Wright and B. L. Adams, Metall. Trans., 23A (1992)759.
- [2] R. A. Swarzer, Micron, 3 (1997) 249.

- [3] K. Z. Baba-Kishi and D. J. Dingley, *Scanning*, 11 (1989) 305.
- [4] R. P. Goehner and J. R. Michael, *J. of Res. of the Nat. Institute of Standards and Technology*, 101 (1996) 301.
- [5] K. Z. Baba-Kishi, *Scanning*, 20 (1998) 117.
- [6] L. Reimer, *Scanning Electron Microscopy* (Springer, New York, 1974).
- [7] J. M. Cowley, *Diffraction Physics* (North-Holland, Amsterdam, 1990).
- [8] J. R. Michael, M. E. Schlienger and R. P. Goehner, *Microscopy and Microanalysis*, 3 Supplement (1997) 879.
- [9] J. W. Steeds, *Convergent Beam Electron Diffraction*, in: *Introduction to Analytical Electron Microscopy*, eds. J. J. Hren, J. I. Goldstein and D. C. Joy, (Plenum Press, New York, 1979) p. 399.
- [10] M. Raghavan, J. C. Scanlon and J. W. Steeds, *Metall. Trans.*, 15A (1984) 1299.
- [11] J. C. H. Spence and J. M. Zhou, *Electron Microdiffraction* (Plenum Press, New York, 1992).
- [12] P. M. Jones, G. M. Rackham and J. W. Steeds, *Proc. Roy. Soc.*, A354 (1977) 197.
- [13] Y. P. Lin, D. M. Bird and R. Vincent, *Ultramicroscopy*, 27 (1989) 233.
- [14] E. G. Bithell and W. M. Stobbs, *J. Microscopy*, 153 (1989) 233.
- [15] D. M. Bird, *J. Electron Microsc. Tech.*, 13 (1989) 77.

Figure Captions

Figure 1. EBSD pattern from arsenopyrite (AsFeS) collected at 20 kV. Note the large number of HOLZ rings.

Figure 2. EBSD pattern from Galena (PbS) collected at 20 kV. Only a very faint HOLZ ring is visible (see arrow).

Figure 3. EBSD pattern of Cr_7C_3 obtained at 20 kV. The HOLZ ring is indicated by arrows.

Figure 4. EBSD patterns of Hematite at a) 5kV, b) 10kV, c) 20kV, d)25kV and E)30 kV. The $\langle 211 \rangle$ HOLZ ring is indicated by arrows.

Figure 5. EBSD patterns from Mo. The $\langle 111 \rangle$ HOLZ ring is indicated by arrows. a)10 kV, b) 20kV and c)35 kV.

Figure 6. EBSD patterns from W . Arrows indicate the $\langle 111 \rangle$ HOLZ ring. A) 10 kV, b) 20 kV and c)40 kV.

Figure 7. Extrapolation plot for the Mo data shown in Table 4. The solid line is the experimental data and the dashed line is the linear curve fit to the data.

Figure 8. EBSD patterns from two polytypes of SiC along with the correct indexing. Both patterns were acquired at 20 kV. a.) SiC 6H polytype ($a=0.307$ nm, $b= 1.508$ nm) b.) SiC 15R polytype ($a=0.307$ nm , $b=3.770$ nm) c. EBSD pattern from 8a indexed , d.) EBSD pattern from 8b indexed.

Figure A1. Schematic diagram of the Ewald sphere construction for the kinematical radius of the HOLZ ring at a zone axis.

Figure A2. Schematic figure to show the way in which the position of the HOLZ ring is modified by dynamical diffraction in the zero order Laue zone (the zero layer).

Table 1. Layer spacings measured from many crystal systems and compounds at 20 kV.

Specimen	Crystal Structure	[UVW]	Measured H^{-1} (nm)	Calculated H^{-1} (nm)	Difference (calc- meas) %
Mo	Cubic	[113]	0.554	0.522	-6.24
Mo	Cubic	[110]	0.466	0.445	-4.76
Mo	Cubic	[111]	0.295	0.273	-8.29
W	Cubic	[111]	0.312	0.274	-13.97
W	Cubic	[001]	0.364	0.317	-15.00
FeAsS	Monoclinic	[101]	0.956	0.954	-0.20
FeAsS	Monoclinic	[111]	1.122	1.109	-1.15
FeAsS	Monoclinic	[001]	0.591	0.577	-2.21
RuO ₂	Tetragonal	[101]	0.557	0.588	5.27
RuO ₂	Tetragonal	[001]	0.471	0.499	5.69
Mo ₂ C	Hexagonal	[101]	0.569	0.561	-1.31
Mo ₂ C	Hexagonal	[001]	0.476	0.474	-0.61
SiC (6H)	Hexagonal	[241]	1.858	1.846	0.67
SiC (15R)	Rhombohedral	[10 5 1]	1.545	1.538	0.45
Ta	Cubic	[001]	0.366	0.331	-10.56
Fe ₃ C	Orthorhombic	[001]	0.454	0.453	-0.40
Cr ₂₃ C ₆	Cubic	[001]	1.076	1.066	-0.92
Cr ₇ C ₃	Orthorhombic	[001]	0.453	0.453	-0.05
Fe ₂ O ₃	Rhombohedral	[211]	0.544	0.543	-0.31
Ni ₃ P	Tetragonal	[001]	0.432	0.439	1.46
FeCr	Tetragonal	[001]	0.457	0.454	-0.53
HfO ₂	Monoclinic	[001]	0.563	0.529	-6.51
Y ₂ BaCuO ₅	Orthorhombic	[100]	0.454	0.453	-0.40
MnSiO ₃	Triclinic	[001]	0.669	0.671	-0.25

TABLE 2. Measured layer spacing for Cr₇C₃.

Measurement #	2θ (deg)	H (nm ⁻¹)	H ⁻¹ (nm)
1	11.170	2.206	0.4532
2	11.152	2.199	0.4569
3	11.182	2.211	0.4523
4	11.199	2.218	0.4509
5	11.167	2.205	0.4535
6	11.238	2.233	0.4478
7	11.147	2.197	0.4551
8	11.089	2.175	0.4598
		Average	0.453 ± 0.003

Table 3 Reciprocal lattice layer spacings for [211] in Hematite.

kV	H ⁻¹ (nm)	Difference (calc- meas) %
5	0.543	0.054
10	0.549	0.188
20	0.544	0.301
25	0.541	- 0.380
30	0.544	0.192

Table 4. Comparison of layer spacing measurements for Mo [111] as a function of accelerating voltage.

kV	H ⁻¹ (nm)
10	0.303
20	0.295
35	0.286

Actual value for Mo = 0.2726 nm

Table 5. Comparison of layer spacing for W [111] as a function of accelerating voltage.

kV	H ⁻¹ (nm)
10	0.319
20	0.312
40	0.306

Actual value for W = 0.2741 nm

Table 6. Comparison of layer spacing for W [001] as a function of accelerating voltage.

kV	H⁻¹ (nm)
10	0.373
20	0.364
40	0.365

Actual value for W = 0.3165 nm

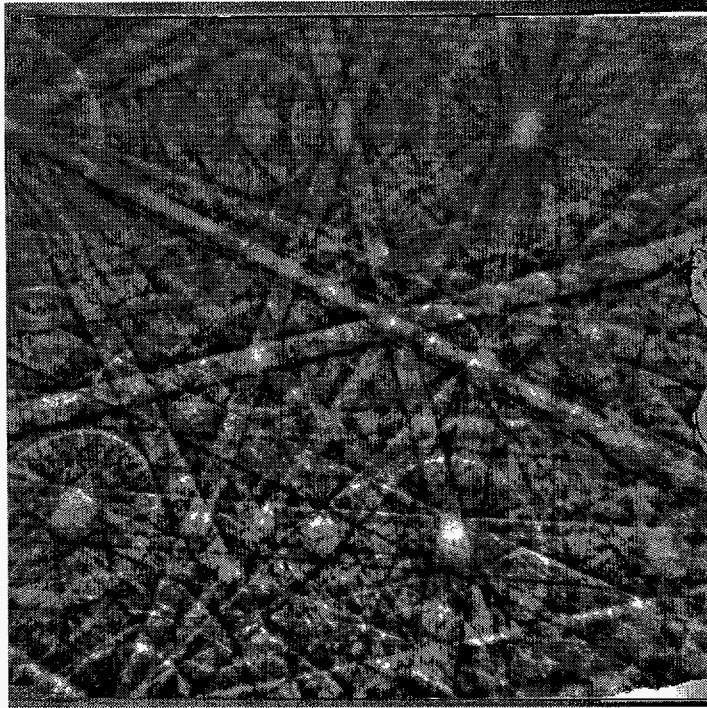


Figure 1. EBSD pattern from arsenopyrite (AsFeS) collected at 20 kV. Note the large number of HOLZ rings.

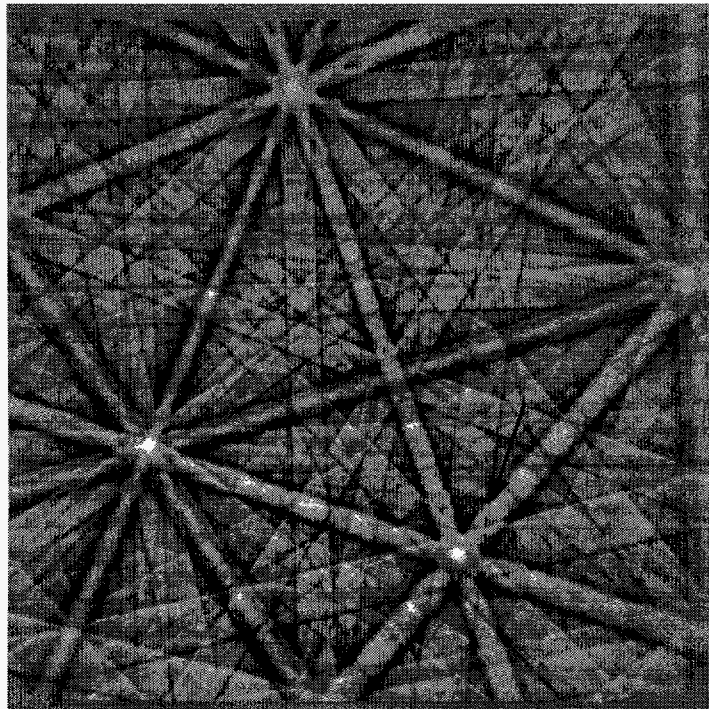


Figure 2. EBSD pattern from Galena (PbS) collected at 20 kV. Only a very faint HOLZ ring is visible (see arrow).

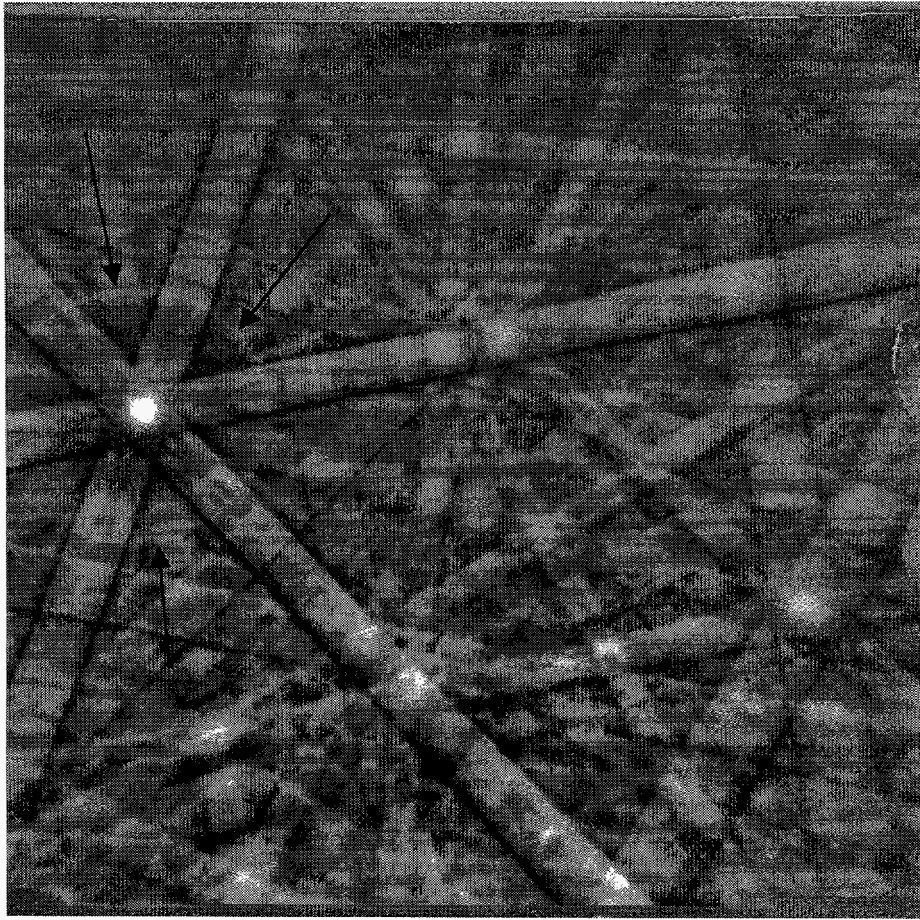


Figure 3. EBSD pattern of Cr_7C_3 obtained at 20 kV. The HOLZ ring is indicated by arrows.

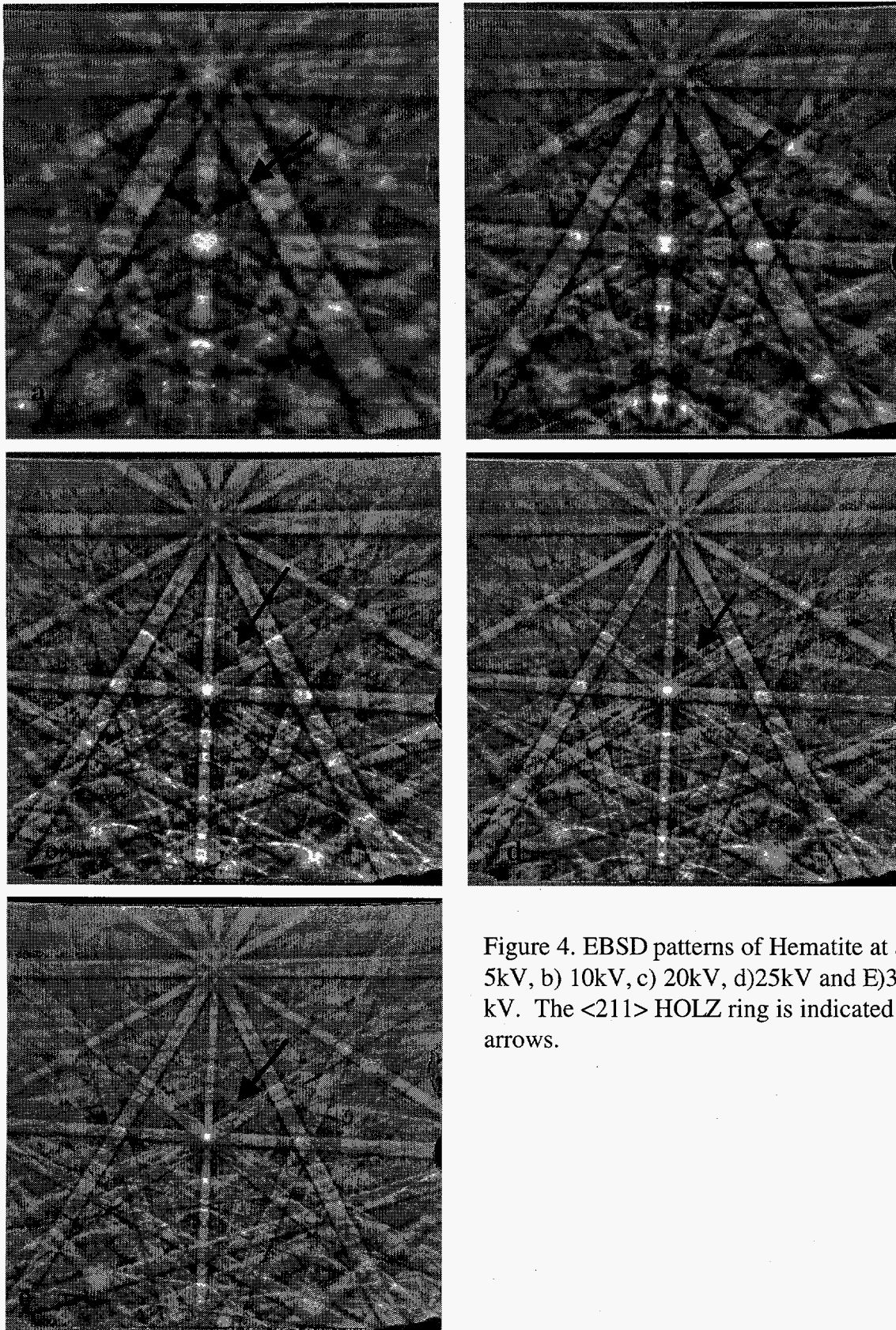


Figure 4. EBSD patterns of Hematite at a) 5kV, b) 10kV, c) 20kV, d)25kV and E)30 kV. The $\langle 211 \rangle$ HOLZ ring is indicated by arrows.

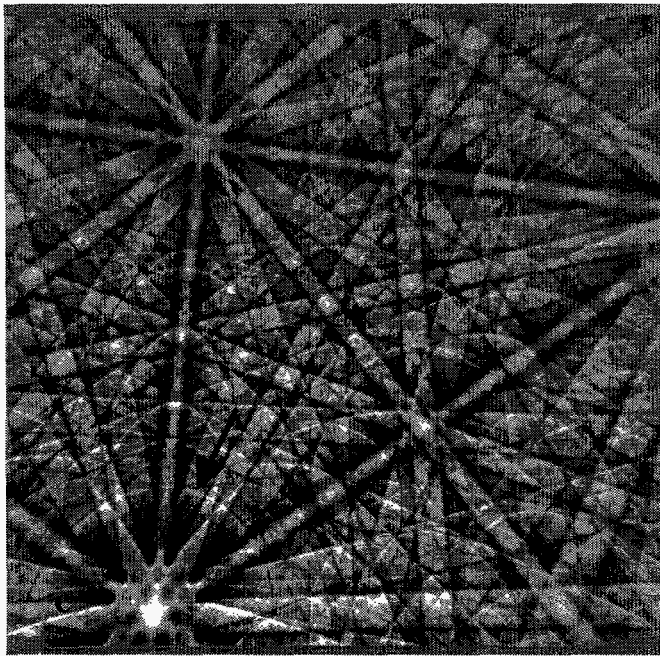
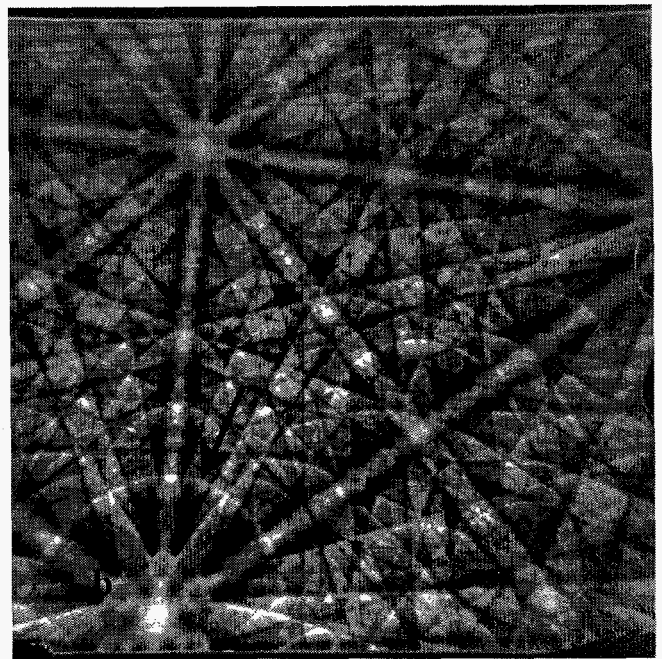
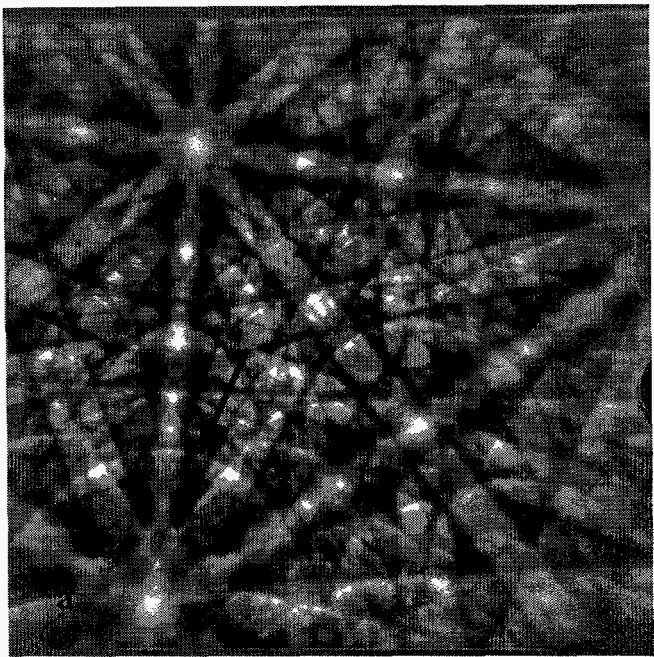


Figure 5. EBSD patterns from Mo. The $\langle 111 \rangle$ HOLZ ring is indicated by arrows. a) 10 kV, b) 20 kV and c) 35 kV.

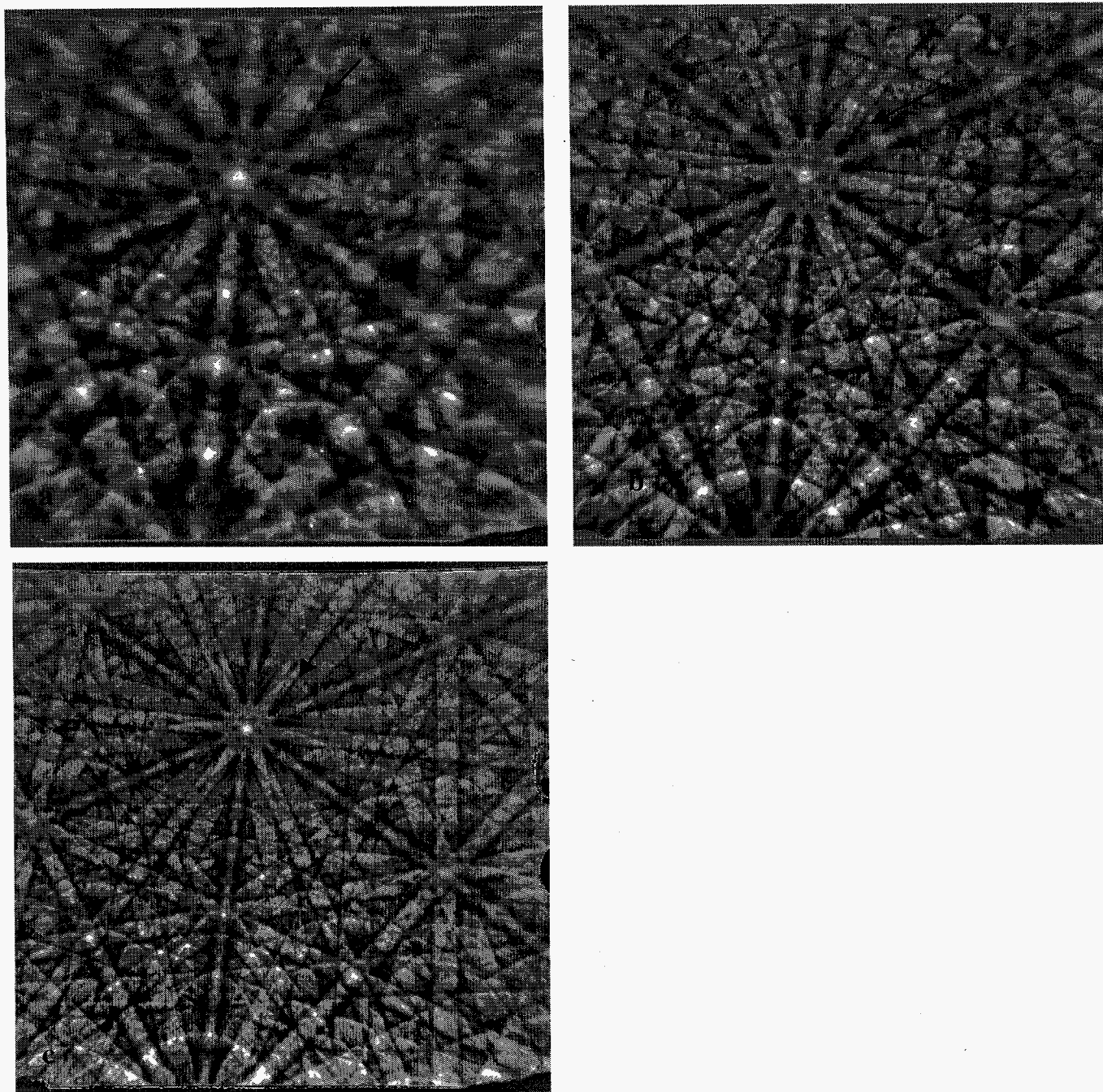


Figure 6. EBSD patterns from W . Arrows indicate the $\langle 111 \rangle$ HOLZ ring. A) 10 kV, b) 20 kV and c) 40 kV.

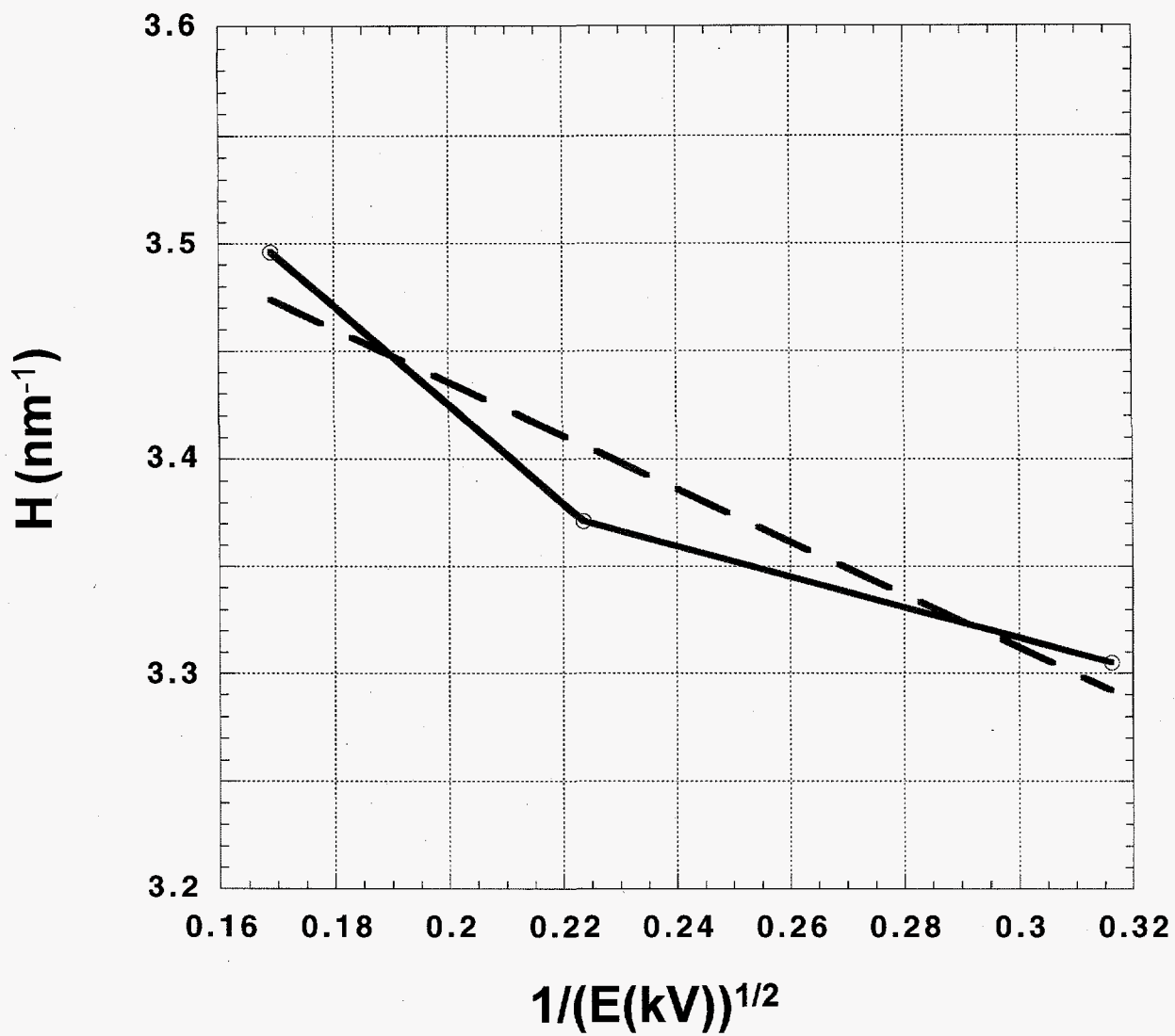


Figure 7. Extrapolation plot for the Mo data shown in Table 4. The solid line is the experimental data and the dashed line is the linear curve fit to the data.

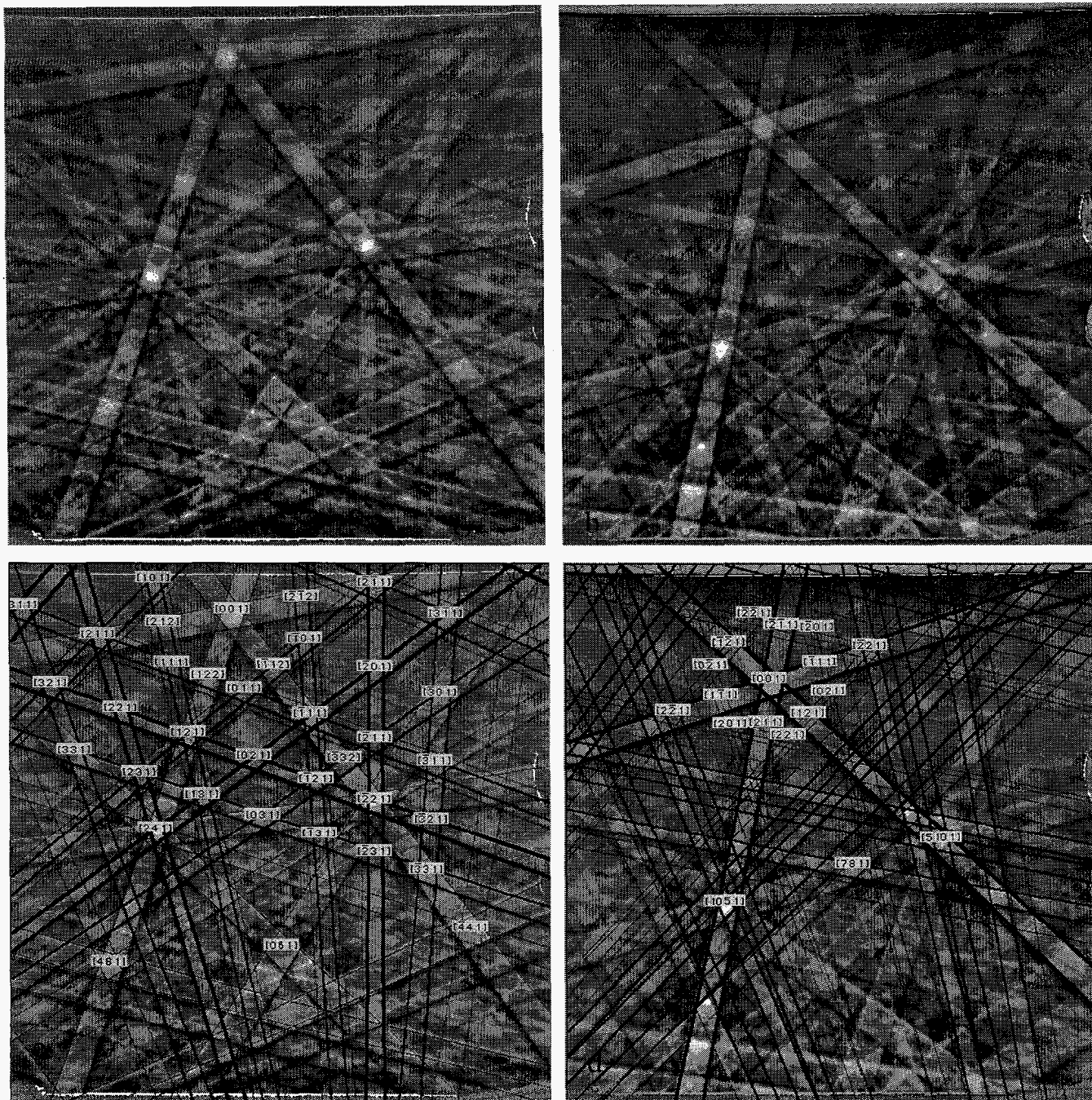


Figure 8. EBSD patterns from two polytypes of SiC along with the correct indexing. Both patterns were acquired at 20 kV. a.) SiC 6H polytype ($a=0.307$ nm, $b= 1.508$ nm) b.) SiC 15R polytype ($a=0.307$ nm , $b=3.770$ nm) c. EBSD pattern from 8a indexed , d.) EBSD pattern from 8b indexed.

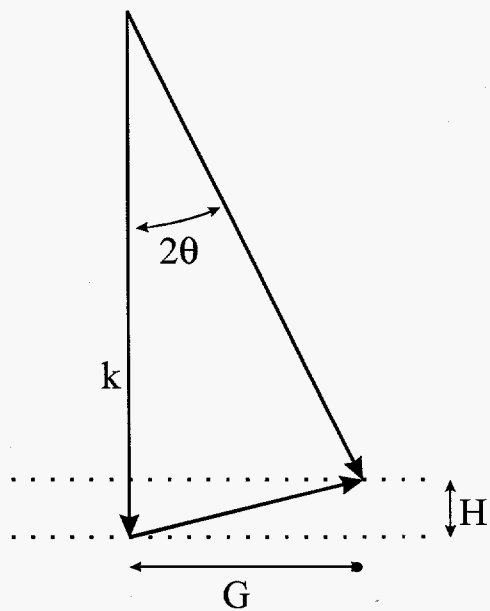


Figure A1. Schematic diagram of the Ewald sphere construction for the kinematical radius of the HOLZ ring at a zone axis.

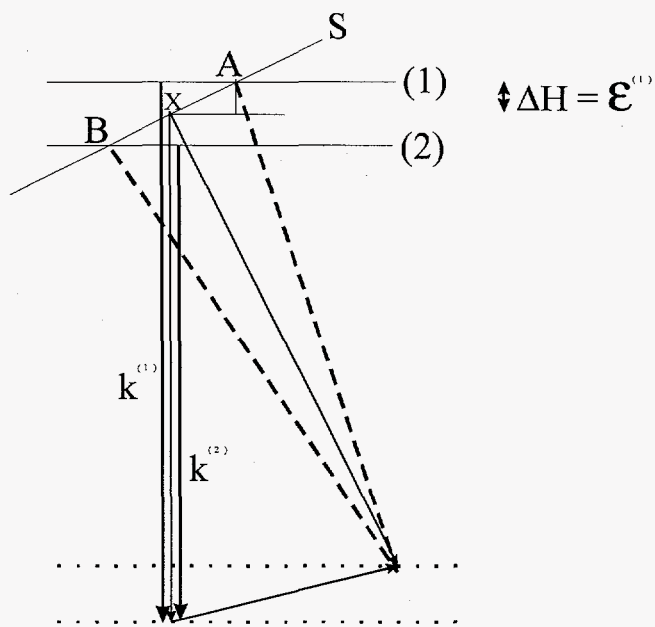


Figure A2. Schematic figure to show the way in which the position of the HOLZ ring is modified by dynamical diffraction in the zero order Laue zone (the zero layer).